Basic Features of the Sunyaev-Zeldovich Effects Relevant to the CCAT

Sunil Golwala

May 27, 2005

Abstract

We discuss various aspects of the Sunyaev-Zeldovich effects relevant to the CCAT. We review the frequency spectrum, make predictions for signal levels and angular sizes from various kinds of objects, and discuss the expected confusion levels.

1 Frequency Spectrum

The thermal Sunyaev-Zeldovich (tSZ) effect consists of a non-thermal distortion of the spectrum of the CMB by Compton scattering through a gas of hot electrons, such as the intracluster medium in galaxy clusters. The thermal SZ effect has now been detected and mapped for about fifty clusters [1]. The spectral signature of the effect (in surface brightness B_ν and thermodynamic temperature T_{CMB}) is

$$\frac{\Delta B_\nu}{B_\nu} = h(x)\,\frac{\Delta T_{\rm CMB}}{T_{\rm CMB}} = h(x)\,f(x)\,y \qquad y = \int n_e\,\frac{k\,T_e}{m_e\,c^2}\,\sigma_T\,dl \tag{1}$$

with

$$B_\nu(x) = 2\,k\,T_{\rm CMB}\left(\frac{\nu}{c}\right)^2\frac{x}{e^x-1} \qquad h(x) = \frac{x\,e^x}{e^x-1} \qquad f(x) = x\frac{e^x+1}{e^x-1} - 4 \tag{2}$$

where $x = h\,\nu/k\,T_{\rm CMB}$ is set by the observing frequency and y is the Comptonization parameter of the scattering medium. k is Boltzmann's constant, m_e, n_e, and T_e are the electron mass, density, and temperature, σ_T is the Thomson scattering cross section, and the integral is along the line of sight. The above expression is valid for nonrelativistic electrons. In most cases, small relativistic corrections are needed. These do not substantially affect our discussion, so we will stick with the simple nonrelativistic expressions.

The kinetic (or kinematic) SZ (kSZ) effect arises from the motion of the scattering medium relative to the CMB rest frame. The scattered radiation experiences a Doppler shift, resulting in a thermal distortion of the spectrum

$$\frac{\Delta B_\nu}{B_\nu} = h(x)\,\frac{\Delta T_{\rm CMB}}{T_{\rm CMB}} = -h(x)\,\frac{v}{c}\,\tau \qquad \tau = \int n_e\,\sigma_T\,dl \tag{3}$$

where v is the peculiar velocity of the scattering medium, c is the speed of light, and τ is the optical depth for Thomson scattering in the ionized medium. Note that the kinetic effect is "thermal" in the sense that the thermodynamic temperature fluctuation is independent of frequency; hence, the kinetic effect is spectrally indistinguishable from primary CMB fluctuations.

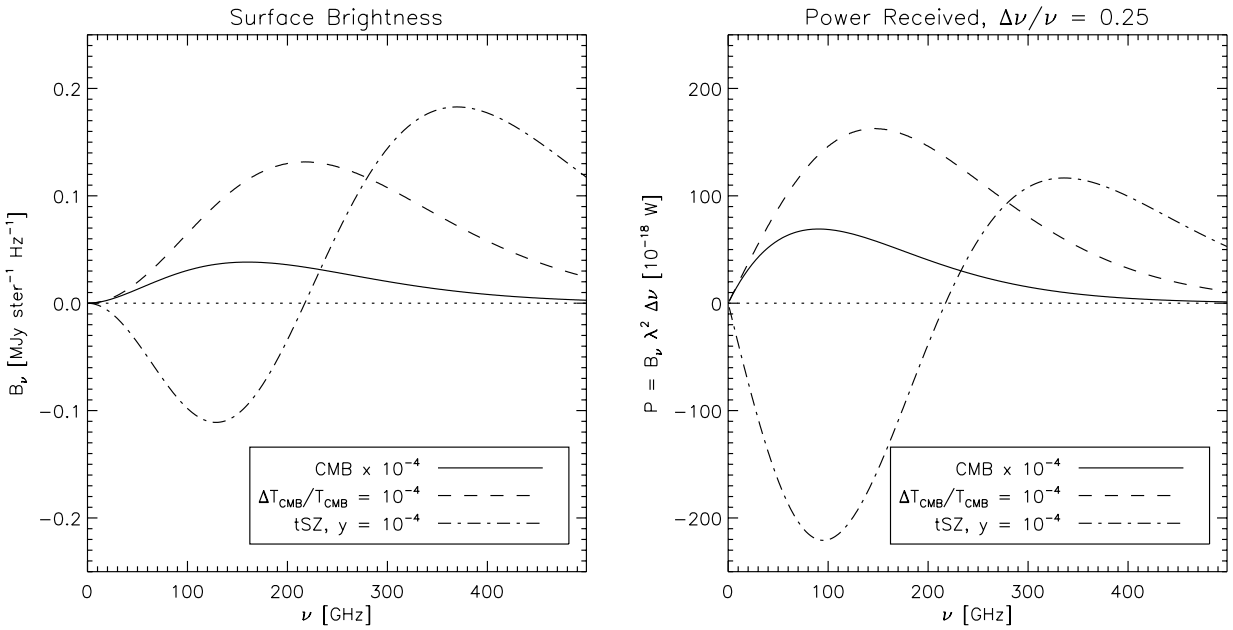

Figure 1: CMB and SZ frequency spectra. Solid curve: CMB. Dashed curve: CMB temperature anistropy at $\Delta T_{\rm CMB}/T_{\rm CMB} = 10^{-4}$ (comparable to primary anisotropy on 1 degree angular scales). Dash-dot curve: thermal SZ (tSZ) effect for $y = 10^{-4}$ ($\tau = 0.005$ and $T_e \sim 10$ keV $\approx 0.02\, m_e\, c^2$), typical of a massive, nearby cluster. The dashed curve also holds for kinetic SZ (kSZ) with $(v/c)\,\tau = 10^{-4}$ (a massive cluster with $\tau = 0.005$ and $v = 600$ km/s, larger than expected by a factor of a few). Right: power incident on a receiver assuming 25% fractional bandwidth and single-optical-mode design.

The frequency spectra of the above two effects, as well as of the microwave background itself, are shown in Figure 1. Note that the spectrum of CMB temperature anisotropy (and similarly of the kinetic effect) differs from that of the CMB itself because the latter is $B_\nu^{\rm CMB}$ while the former is proportional to $dB_\nu^{\rm CMB}/dT_{\rm CMB}$. The figure also shows a more practically useful quantity, the power incident on a single-moded receiver with 25% fractional bandwidth. This incorporates two facts: the optical throughput for a single-moded system is proportional to λ^2 and thus decreases with increasing frequency; and fixed fractional bandwidth yields increasing absolute bandwidth with increasing frequency. The message of the second plot is that one should not be misled by the first plot: though the surface brightness of CMB and SZ fluctuations peak at roughly 220 GHz and 370 GHz, respectively, the received power peaks at smaller frequencies, 150 GHz and 95 GHz, respectively. Since receiver noise-equivalent power for ground-based receivers tends to degrade with increasing frequency (due to increased photon noise from the atmospheric optical loading), one tends to be pushed to lower frequency to obtain the best CMB and SZ sensitivity. This is in contrast to galactic or extragalactic dusty sources, whose surface brightess spectra increase sufficiently steeply with frequency to beat the effects of decreased throughput and increased photon noise.

2 Generic Discussion of the Calculation of Cluster Parameters

Obviously, to gauge the detectability of various SZ signals, we need some idea of what clusters look like in the SZ, and thus relations between SZ profiles and cluster mass, redshift, etc. This requires some simplistic modeling of clusters, in the same way that modeling of galaxies provides us with expected number counts in the submillimeter.

Since we are doing a feasibility study, we are less interested in detailed profiles than we are in typical signal levels and angular scales and how these observables scale with halo mass, formation redshift, etc. These will help us understand how to make tradeoffs to optimize the telescope for specific science goals. So, rather than trying to summarize the most accurate expectations for cluster profiles obtained from the latest simulations and observations, we model the halo dark matter and gas profiles simplistically and "prescriptively" – that is, using perhaps somewhat unmotivated prescriptions that are found to reproduce current simulation work well. The advantage of this approach is that we obtain results that clearly display the dependences of the tSZ signal on halo parameters. We pin our calculations to reality using simulations that relate the integrated thermal SZ flux to the cluster mass, which essentially provide a normalization for the gas and Comptonization profiles.

2.1 Dark Matter Profiles

We begin with the standard technique of using the Navarro-Frenk-White profile [2] of the cluster mass density (derived from simulations):

$$\rho(r) = \frac{\rho_s}{\frac{r}{r_s}\left(1+\frac{r}{r_s}\right)^2} \tag{4}$$

r_s is the "scale radius", where the density function changes power-law slope. ρ_s is just a normalizing parameter. The total mass of a NFW profile diverges logarithmically, so it is necessary to put in a cutoff radius to obtain a finite mass. It is conventional to use the virial radius as the cutoff; the virial mass is obtained by integrating the profile out to this cutoff, giving

$$M_v = \frac{4}{3}\,\pi\,\rho_s\,r_s^3\left[\log\left(1+c_h\right) - \frac{c_h}{1+c_h}\right] \tag{5}$$

here $c_h = R_v/r_s$ is the halo "concentration" parameter. The halo is entirely specified by r_s, R_v, and M_v, or alternatively c_h, R_v, and M_v (or alternatively, a parameter set involving ρ_s instead).

The freedom in the NFW profile is greatly reduced by applying what we know about gravitational collapse. Simple spherical collapse relates the virial radius to the virial mass via[1]

$$M_v = \frac{4}{3}\,\pi\,R_v^3\,\left[1+\delta_{coll,non}(\Omega_{m0},\Omega_{\Lambda 0},z_f)\right]\rho_{b0}\,(1+z_f)^3 \tag{6}$$

where ρ_{b0} is the current ($z=0$) average mass density of the universe, z_f is the redshift of formation of the cluster, and $\delta_{coll,non}(\Omega_{m0},\Omega_{\Lambda 0},z_f)$ is the nonlinear density constrast at the time of formation

[1]The formula arises as follows. $\rho_{b0}\,(1+z_f)^3$ is the physical density at the time cluster formed. $\delta_{coll,non}$ is the nonlinear overdensity at the time of virialization. It is calculated by tracking the evolution of a collapsing sphere of matter in a particular background cosmology.; it is the traditional $18\,\pi^2 \approx 178$ in a $\Omega_m = 1$ flat universe. Thus, $[1+\delta_{coll,non}]\,\rho_{b0}\,(1+z_f)^3$ is the physical density at the time of collapse, which gives us the density to multiply against the virial volume to obtain the mass. Once virialization occurs, the cluster's density and virial radius remain fixed (the halo has decoupled from the expansion of the universe).

for an object that forms at redshift z_f in a universe whose $z = 0$ matter and vacuum energy density parameters are Ω_{m0} and $\Omega_{\Lambda 0}$.[2]

Many authors have studied the behavior of the halo concentration parameter. It seems that the best understanding is provided using full simulations of halo formation [4, 5], wherein the halo concentration parameter c_h is seen to obey $c_h = K\,(1+z_f)\,/\,(1+z_o)$ where z_f and z_o are the redshift of formation of the object and the redshift at which it is observed. K is a constant, dependent on the cosmology. Thus, the concentration at formation is a universal constant (for the given cosmology), and variations in concentration arise due to evolution of the halo between formation and observation. The problem with using this form is that the formation redshift z_f is defined in [4, 5] using the full accretion history of the halo under study; it is not simply the redshift at which the overdensity reaches the critical value for collapse. It is thus difficult to apply their analysis to our rather simplistic picture of cluster formation.

Bullock *et al.* [6] take a different approach. They find that, at any given redshift of observation, the halo concentration parameter of the ensemble of halos has a well-defined mean value with some scatter. The mean value is mildly dependent on mass. As quoted by Cooray [7], the mean value is

$$c_h\,(z_o) = \frac{K}{1+z_o}\left(\frac{M_v}{M_{coll}(z_o)}\right)^{-0.13} \tag{7}$$

where z_o is the redshift at which the halo is observed and $K = 9$. $M_{coll}(z_o)$ is, heuristically, the typical halo mass that is forming at the redshift z_o.[3] Along with this mean value, the halo concentration parameter is seen to be log-normal distributed with $\sigma_{\log c_h} = 0.18$. The scatter in halo concentration parameters has been understood to reflect primarily variation in formation redshift [4, 5].

Seljak [8] used a similar approach but found a simpler behavior was satisfactory. As quoted by Komatsu and Seljak [9], the concentration parameter obeys

$$c_h\,(z_o) = \frac{K}{1+z_o}\left(\frac{M_v}{10^{14}h^{-1}\ \mathrm{M}_\odot}\right)^{-1/5} \tag{8}$$

with $K = 6$. For our purposes, we will use this form, neglecting the scatter in the halo concentration parameter.

Using the halo concentration parameter, the NFW scale radius is therefore related to the mass by

$$M_v\left(\frac{M_v}{10^{14}h^{-1}\ \mathrm{M}_\odot}\right)^{1/5} = \frac{4}{3}\,\pi\,K^3\,r_s^3\,[1+\delta_{coll,non}(\Omega_{m0},\Omega_{\Lambda 0},z_f)]\,\rho_{b0}\left(\frac{1+z_f}{1+z_o}\right)^3 \tag{9}$$

[2] A fitting formula for this collapse overdensity for the case $\Omega_{m0} \le 1, \Omega_{m0}+\Omega_{\Lambda 0} = 1$ is given in [3] and is $\delta_{coll,non}(\Omega_{m0},\Omega_{\Lambda 0} = 1-\Omega_{m0},z) = 18\pi^2\left[1+0.4093\,x^{2.71572}\right]$ with $x = \left(\Omega_{m0}^{-1}-1\right)^{1/3}/\,(1+z)$. One frequently sees the approximation $\delta_{coll,non}(\Omega_{m0},\Omega_{\Lambda 0} = 1-\Omega_{m0},z) = 18\pi^2\,[\Omega_m(z)]^{-0.55}$, with $\Omega_m(z) = \left[\Omega_{m0}\,(1+z)^3\right]/\left[\Omega_{m0}\,(1+z)^3+\Omega_{\Lambda 0}\right]$ (also valid only for a flat universe!), which is good to 5-10% at low z, better at $z > 1$.

[3] More technically, $M_{coll}(z_o)$ is obtained from Press-Schechter theory as follows. At any given redshift z_o, we may smooth the linear density field with a top hat of radius R_t. The smoothed density field will have some rms value $\sigma(R_t;z_o) = \sigma(M_t;z_o)$ where $M_t = \frac{4\pi}{3}\,R_t^3\,\rho_b(z_o)$ is the typical mass associated with the top hat radius R_t and σ is determined by the details of the primordial power spectrum and the structure growth function for the given cosmology. This smoothed density field has a Gaussian distribution of overdensities. There is a critical linear overdensity for collapse, $\delta_{coll,lin}(z)$, which is redshift- and cosmology-dependent, but is exactly $(3/20)(12\,\pi)^{2/3} \approx 1.686$ in an Einstein-deSitter universe and negligibly different in other universes. Excursions of the smoothed density field with overdensity greater than this value collapse and form halos. For the given redshift, there is exactly one R_t for which the rms of the overdensity distribution exactly matches the linear collapse overdensity. The mass of the collapsing objects on this length scale (with mass $M = 1.686\,M_t$) is $M_{coll}(z_o)$.

Thus, the algorithm for obtaining a full halo profile for a cluster of a specified virial mass M_v, formation redshift z_f, and observation redshift z_o is:

1. Specify the virial mass M_v and a redshift of formation z_f.
2. Obtain R_v from M_v, z_f, and Equation 6.
3. Obtain r_s from R_v, z_f, z_o and Equation 8.
4. Obtain ρ_s from M_v, R_v, r_s and Equation 5.

2.2 Gas Profiles

Since the SZ effects arise from Compton scattering of the CMB by the intracluster plasma, we next require some information about the gas profile of the cluster. One that is typically used is the isothermal beta profile with $\beta = 2/3$, which approximates well the actual profile obtained by assuming hydrostatic equilibrium if one takes $r_c = 0.2\,r_s$ for the relationship between the beta profile core radius r_c and the NFW scale radius r_s.[4] We define the "gas concentration factor" to be $c_g = r_s/r_c$. While the details of the relation between the beta profile and the "true" profile will of course vary as one includes more astrophysics, we use the simple $\beta = 2/3$ and $r_c = 0.2\,r_s$ profile in the general spirit of our approximation. We keep the parameter c_g explicit until we make numerical calculations. More physically motivated profiles can be found in [10, 7, 11, 9, 12].

A beta model gas density profile obeys

$$\rho_g(r) = \rho_{g0}\left[1 + \left(\frac{r}{r_c}\right)^2\right]^{-3\beta/2} \tag{10}$$

$$= \frac{\rho_{g0}}{1 + \left(\frac{r}{r_c}\right)^2} \qquad \text{for } \beta = 2/3 \tag{11}$$

The normalization is set by requiring that the total gas mass enclosed within the virial radius be related to the total halo mass by the universal baryon fraction f_b.[5] For the beta model, the Comptonization parameter has the analytical form [13]

$$y(r) = y_0\left[1 + \left(\frac{r}{r_c}\right)^2\right]^{(1-3\beta)/2} \qquad y_0 = \tau_0\,\frac{k\,T_e}{m_e\,c^2} \qquad \tau_0 = \frac{\rho_{g0}}{\mu\,m_p}\,\sigma_T\,r_c\,\sqrt{\pi}\,\frac{\Gamma(\frac{3}{2}\beta - \frac{1}{2})}{\Gamma(\frac{3}{2}\beta)} \tag{12}$$

which, for the simple $\beta = 2/3$ model, reduces to

$$y(r) = y_0\left[1 + \left(\frac{r}{r_c}\right)^2\right]^{-1/2} \qquad \tau_0 = \frac{\rho_{g0}}{\mu\,m_p}\,\sigma_T\,r_c \tag{13}$$

We will see later that it is useful to also have the integral of y over radius. This can be calculated analytically:

$$Y(r) = 2\,\pi\int_0^r y(r')\,r'\,dr' = 2\,\pi\,y_0\int_0^r \frac{r'\,dr'}{\left[1 + \left(\frac{r'}{r_c}\right)^2\right]^{1/2}} = 2\,\pi\,y_0\,r_c^2\left[1 + \left(\frac{r}{r_c}\right)^2\right]^{1/2} \tag{14}$$

[4] It turns out that assuming this relationship $r_c = 0.2\,r_s$ only affects the central part of the profile, making the y and τ profiles' core radius smaller and increasing their peak value. At large radii, the two effects largely cancel, so the SZ signals in the wings of the cluster only weakly depend on what relationship one assumes between r_c and r_s.

[5] Again, a prescription. This ratio is expected to hold in the outer wings of the cluster (Komatsu and Seljak [9]), but we assume it holds true globally for simplicity.

So, in particular, integrating y out to the virial radius gives

$$Y_v = Y(R_v) = 2\,\pi\,y_0\,r_c^2\left[1+\left(\frac{R_v}{r_c}\right)^2\right]^{1/2} = 2\,\pi\,y_0\,\frac{R_v^2}{c_h^2}\frac{1}{c_g^2}\sqrt{1+c_h^2c_g^2} \tag{15}$$

where we have obtained the second form so that the relationship is parameterized in terms of R_v, the halo concentration parameter c_h, and the gas concentration parameter c_g. R_v is determined only by the halo mass and the background cosmology. c_h is determined by the details of dark matter halo collapse and is obtained from simulations. The gas concentration parameter c_g depends on details of the gas physics. The second form thus makes it easy to see where changes in physical assumptions would have an effect.

Y_v can also be rewritten in a suggestive form by rewriting only in terms of R_v and r_c:

$$y_0 = \frac{Y_v/2}{\pi\,r_g^2} \qquad r_g^2 = r_c\,\sqrt{r_c^2+R_v^2} \approx r_c\,R_v \tag{16}$$

That is, y_0 can be interpreted as the mean value of y obtained by taking half of Y_v and spreading it over a disk whose radius is approximately r_g, the geometric mean of r_c and R_v, or, alternatively, spreading all of Y_v over a disk whose radius is $\sqrt{2}$ times r_g. The geometric mean, r_g, of the two radii can thus be interpreted as the effective radius of the signal. It is a more appropriate radius than either r_c or R_v, which are, respectively too small (containing only the peak of the profile) and too large (containing the entire y profile, but most of the area has low y).

Let us convert the various radii we have calculated to angles so we get an idea of the angular scales of interest. We simply apply the angular diameter distance to R_v and obtain θ_c and θ_g from θ_v via the halo concentration parameter c_h and the gas concentration parameter c_g. Note that we calculate the angular diameter distance to the redshift of observation, z_o, not the redshift of formation z_f:

$$\theta_v = \frac{R_v}{d_A(z_o)} = \frac{1}{c/H_0}\frac{c/H_0}{d_A(z_o)}\frac{M_v^{1/3}}{(1+z_f)}\left[\frac{3}{4\,\pi\,\rho_{b0}\,(1+\delta_{coll,non}(\Omega_{m0},\Omega_{\Lambda 0},z_f))}\right]^{1/3} \tag{17}$$

$$= \frac{1.5}{3000}\,h\,\frac{c/H_0}{d_A(z_o)}\,(1+z_f)^{-1}\left(\frac{M_v}{10^{14}\ M_\odot}\right)^{1/3} \tag{18}$$

$$= 1.2\,\frac{c/H_0}{d_A(z_o)}\,(1+z_f)^{-1}\left(\frac{M_v}{10^{14}\ M_\odot}\right)^{1/3}\ \text{arcmin} \tag{19}$$

$$\theta_c = \frac{1}{c_g}\,\frac{\theta_v}{c_h(z_o)} = \frac{1}{c_g}\,\theta_v\frac{1+z_o}{K}\left(\frac{M_v}{10^{14}h^{-1}\ \mathrm{M}_\odot}\right)^{1/5} \tag{20}$$

$$= 0.03\,h^{1/5}\frac{c/H_0}{d_A(z_o)}\,\frac{1+z_o}{1+z_f}\,\left(\frac{M_v}{10^{14}\ M_\odot}\right)^{8/15}\ \text{arcmin} \tag{21}$$

$$\theta_g \approx \sqrt{\theta_s\,\theta_v} \tag{22}$$

$$= 0.18\,h^{1/10}\frac{c/H_0}{d_A(z_o)}\frac{(1+z_o)^{1/2}}{1+z_f}\left(\frac{M_v}{10^{14}\ M_\odot}\right)^{13/30}\ \text{arcmin} \tag{23}$$

The factor $(c/H_0)\,/d_A(z_o)$ is in the range 2.5 to 5 for $z > 0.25$ in a ΛCDM universe, taking on its largest value at $z = 0.25$.

2.3 Normalization of the Gas Density and Optical Depth Profile using the Universal Baryon Fraction

For normalization of the gas density profile (and therefore the optical depth), we can simply require that the gas mass of the cluster match the universal baryon fraction.

The central optical depth was found earlier (Equation 13) to be

$$\tau_0 = \frac{\rho_{g0}}{\mu\, m_p}\, \sigma_T\, r_c \tag{24}$$

where ρ_{g0} is the central gas density. The central gas density can be found by integrating the gas mass and requiring that it be a fraction f_b of the total mass, where f_b is the universal baryon fraction (we neglect niceties about whether it should be f_b or $f_b/(1+f_b)$.) The integral is

$$M_g = 4\,\pi\,\rho_{g0} \int_0^{R_v} \frac{r^2\, dr}{1+\left(\frac{r}{r_c}\right)^2} = 4\,\pi\,\rho_{g0}\, r_c^3\, [x - \arctan x]|_0^{R_v/r_c} \tag{25}$$

$$= 4\,\pi\,\rho_{g0}\, r_c^3 \left[\frac{R_v}{r_c} - \arctan\frac{R_v}{r_c}\right] \tag{26}$$

$$= 4\,\pi\,\rho_{g0}\, r_c^3\, [c_h c_g - \arctan c_h c_g] \tag{27}$$

where c_h is the halo concentration parameter, r_c is the gas profile core radius, and c_g is the gas concentration parameter. Therefore,

$$\tau_0 = \frac{\sigma_T}{4\,\pi\,\mu\, m_p}\, \frac{f_b\, M_v}{r_c^2}\, \frac{1}{c_h c_g - \arctan c_h c_g} \tag{28}$$

r_c can be rewritten in terms of r_s, and r_s in terms of M_v using Equation 9, which allows us to rewrite τ_0:

$$\tau_0 = \left(\frac{1}{36\,\pi}\right)^{1/3} \sigma_T\, f_b\, K^2 c_g^2\, \left([1+\delta_{coll,non}(\Omega_{m0},\Omega_{\Lambda 0},z_f)]\,\rho_{b0}\right)^{2/3} M_v^{1/3}\, \frac{1+z_f}{1+z_o}\, \frac{M_{14hinv}^{-2/5}}{c_h c_g - \arctan c_h c_g} \tag{29}$$

$$= \left(\frac{1}{36\,\pi}\right)^{1/3} \sigma_T\, f_b\, K\, c_g\, \left([1+\delta_{coll,non}(\Omega_{m0},\Omega_{\Lambda 0},z_f)]\,\rho_{b0}\right)^{2/3} \frac{M_v^{1/3}\, M_{14hinv}^{-1/5}}{1 - \frac{\arctan c_g \frac{K}{1+z_o} M_{14hinv}^{-1/5}}{c_g \frac{K}{1+z_o} M_{14hinv}^{-1/5}}}\, (1+z_f) \tag{30}$$

where $M_{14hinv} = M_v/10^{14} h^{-1}\ \mathrm{M}_\odot$. Inserting the numbers (we take $f_b = 0.06\, h^{-1.5} = 0.10$ and fix $h = 0.71$ because the dependence on it is weak), we find

$$\boxed{\tau_0 = 1.5\ \times\ 10^{-3}\, \left(\frac{M}{10^{14}\ \mathrm{M}_\odot}\right)^{2/15}\, \frac{1+z_f}{1 - \frac{\arctan c_g \frac{K}{1+z_o} M_{14hinv}^{-1/5}}{c_g \frac{K}{1+z_o} M_{14hinv}^{-1/5}}}} \tag{31}$$

The concentration-dependent factor varies between approximately 1 and 1.2 for $z_o < 3$, so the redshift-dependent factors do not change the optical depth by much.[6]

[6] As a check, we note that CL0016+16 is quoted by Birkinshaw [13] to have an optical depth of about 0.01. The

2.4 Normalization of Comptonization Profile using Simulations

For the y profile, which is dependent on the electron temperature, we abandon adiabatic collapse and instead base the normalization on simulations. It is usually found [15, 16] that the central Comptonization parameter (y at the center of the cluster, usually known as y_0) is strongly dependent on details of cluster astrophysics such as recent mergers, entropy injection, etc. A more robust observable is the integral of the tSZ signal over the cluster face. This is usually written as the integral of the tSZ "flux density" over the cluster face (in quotes because it can be a negative flux density at low frequencies):

$$S_\nu = \int d^2\theta \, \Delta B_\nu(\vec{\theta}) = B_\nu(x) \, h(x) \, f(x) \int d^2\theta \, y(\vec{\theta}) \tag{32}$$

$$= B_\nu(x) \, h(x) \, f(x) \int d^2\theta \, dl \, n_e(\vec{\theta}, l) \, \sigma_T \, \frac{k \, T_e}{m_e \, c^2} \tag{33}$$

$$= B_\nu(x) \, h(x) \, f(x) \, \frac{\sigma_T}{d_A^2(z)} \int d^3l \, n_e(\vec{l}) \, \frac{k \, T_e}{m_e \, c^2} \tag{34}$$

$$= B_\nu(x) \, h(x) \, f(x) \, \frac{\sigma_T}{d_A^2(z)} \, \frac{k \, \langle T_e \rangle_n}{m_e \, c^2} \, N_e \tag{35}$$

$$= B_\nu(x) \, h(x) \, f(x) \, \frac{\sigma_T}{d_A^2(z)} \, \frac{k \, \langle T_e \rangle_n}{m_e \, c^2} \, \frac{M \, f_b}{\mu \, m_p} \tag{36}$$

where $B_\nu(x)$ is the Planck blackbody function at $x = h\,\nu / k\,T_{\rm CMB}$, $f(x)$ and $h(x)$ are the additional frequency dependent factors given in Section 1, $d_A(z)$ is the angular diameter distance to redshift z, σ_T is the Thomson cross-section, $\langle T_e \rangle_n$ is the number-weighted mean electron temperature, M is the cluster mass, f_b is the baryonic fraction, μ is the mean atomic weight of the intracluster plasma, and m_p is the proton mass. Basic Press-Schecter theory, as well as numerical simulations, show that the redshift dependences of T_e and $d_A(z)$ largely cancel so that there is an approximately one-to-one relationship between S_ν and M.[7] This relationship can be modified somewhat by radiative cooling or entropy injection, but these effects have been checked and seen to affect the relation by less than a factor of 2 [16, 17].

It is useful to factorize the above expression. Let

$$Y_{\rm Mpc^2} = \sigma_T \int d^3l \, n_e(\vec{l}) \, \frac{k \, T_e}{m_e \, c^2} \tag{37}$$

$Y_{\rm Mpc^2}$ contains only those pieces of the expression intrinsic to the cluster. The flux density is then written as

$$S_\nu = B_\nu(x) \, h(x) \, f(x) \, \frac{Y_{\rm Mpc^2}}{d_A^2(z)} \tag{38}$$

It is also conventional to use

$$Y = \int d^2\theta \, y(\vec{\theta}) = \frac{Y_{\rm Mpc^2}}{d_A^2(z)} \qquad S_\nu = B_\nu(x) \, h(x) \, f(x) \, Y \tag{39}$$

cluster has a total mass inside 3 Mpc of 2.3×10^{15} $M_\odot$ [14]. The above formula yields 0.0023 for the prefactor, ignoring the factor with the redshift dependence. The redshift dependence could easily bring in another factor of 2. The remaining factor of 2 discrepancy could be explained by claiming that the mass estimate is too low. A cluster of this mass should have $c_h \, c_g \approx 17$, whereas the gas core radius is only 300 kpc, suggesting the virial radius is at least 5 Mpc, not the 3 Mpc inside of which the mass has been counted. Including the mass out to the larger radius would push up the mass estimate, resulting in higher τ_0. So our formula seems to be not too far off from the data.

[7] For self-similar evolution (flat, $\Omega_m = 1$ universe), we expect $T \propto (1+z)$, so $S \propto d_A^{-2} \, T \propto d_A^{-2} \, (1+z)$. One sees empirically that this function varies by less than a factor of 2 over the redshift range $z = 0.5$ to $z = 2.5$.

though we will not find these latter expressions useful here.

We will work with the relation between $Y_{\rm Mpc^2}$ and M obtained via simulations by da Silva *et al.* [17]. Specifically, we will use their "cooling" fit because it is somewhat conservative to do so – it tends to produce a shallower $Y_{\rm Mpc^2}$ vs. M relation than "adiabatic" and "preheating" models.[8] They calculate $Y^{200}_{\rm Mpc^2}$, which is $Y_{\rm Mpc^2}$ integrated out to the radius at which the enclosed density was 200 times the critical density of the universe at the time of virialization.[9] They find

$$Y^{200}_{\rm Mpc^2}(M_{200}, z_f) \approx 10^{-6}\,(1+z_f)^{1.14}\left(\frac{M_{200}}{10^{14}\ h^{-1}M_\odot}\right)^{1.83}\ \left(h^{-1}\,{\rm Mpc}\right)^2 \tag{40}$$

where z_f is the redshift of "formation".[10]

If the da Silva formula were in terms of Y_v and M_v, we could obtain y_0 easily and thus have the full y profile. However, da Silva provides $Y^{200}_{\rm Mpc^2}$ and M_{200}, so we have to rewrite these in terms of virial quantities. M_{200} and R_{200} are defined as the mass enclosed within the radius at which the average density of the enclosed material is 200 times that of the critical density. Thus, the two are related by (for a flat universe, only!):

$$M_{200} = \frac{4}{3}\,\pi\,R^3_{200}\,[200]\ \rho_{crit}(z_f) = \frac{4}{3}\,\pi\,R^3_{200}\,[200]\ \frac{\rho_{b0}}{\Omega_{m0}}\left[\Omega_{m0}\,(1+z_f)^3 + \Omega_{\Lambda 0}\right] \tag{41}$$

Using the NFW profile, they are also related by

$$M_{200} = \frac{4}{3}\,\pi\,\rho_s\,r_s^3\left[\log\left(1+\frac{R_{200}}{r_s}\right) - \frac{R_{200}}{r_s+R_{200}}\right] \tag{42}$$

We can rewrite the above in terms of M_v and R_v only by dividing by the analogous relations between virial quantities

$$\frac{M_{200}}{M_v} = \left(\frac{R_{200}}{R_v}\right)^3 \frac{200}{1+\delta_{coll,non}(\Omega_{m0},\Omega_{\Lambda 0},z_f)}\,\frac{\left[\Omega_{m0}\,(1+z_f)^3+\Omega_{\Lambda 0}\right]}{\Omega_{m0}\,(1+z_f)^3} \tag{43}$$

$$\frac{M_{200}}{M_v} = \frac{\left[\log\left(1+\frac{R_{200}}{r_s}\right) - \frac{R_{200}}{r_s+R_{200}}\right]}{\left[\log\left(1+c_h\right) - \frac{c_h}{1+c_h}\right]} = \frac{\left[\log\left(1+c_h\,\frac{R_{200}}{R_v}\right) - \frac{c\,R_{200}/R_v}{1+c_h\,R_{200}/R_v}\right]}{\left[\log\left(1+c_h\right) - \frac{c_h}{1+c_h}\right]} \tag{44}$$

Clearly, we could combine the two equations to obtain a transcendental relationship between R_{200} and R_v, and thereby find M_{200}. However, for the accuracy of approximation we are interested in, the distinction between virial and "200" masses is likely small enough to ignore. So we replace "200" quantities in the da Silva relation with virial ones.

Let us now obtain the normalization of the y profile, y_0. Using Equations 40, 6, and 15, we

[8] Specifically (referring to equations, tables, and figures in [17]), we take Equation 17, use the "cooling" values for α_M and β_M from Table 2, and use Equation 12 to give the normalization at $z = 0$. The behavior of β_M vs. z_f in Figure 6 is thereby reproduced. There is no evidence for evolution of α_M with z.

[9] This definition is a bit unexpected – note that the definition refers to the *critical* density, not the background density.

[10] "Formation" of a cluster is equivalent to virialization or collapse, and is conventionally defined to be the time at which a perfectly spherical mass distribution of the same overdensity would have collapsed to zero radius.

obtain

$$y_0 = \frac{Y_v}{2\,\pi\,R_v^2}\,\frac{c_h^2 c_g^2}{\sqrt{1+c_h^2 c_g^2}} \tag{45}$$

$$= \frac{1}{2\,\pi}\,\frac{c_h^2 c_g^2}{\sqrt{1+c_h^2 c_g^2}}\,\frac{10^{-6}\,(1+z_f)^{1.14}\left(\frac{M_v}{10^{14}\ h^{-1}M_\odot}\right)^{1.83}\ \left(h^{-1}\,\mathrm{Mpc}\right)^2}{M_v^{2/3}\left(\frac{4\,\pi}{3}\,\rho_{b0}\right)^{-2/3}\ (1+z_f)^{-2}\ [1+\delta_{coll,non}(\Omega_{m0},\Omega_{\Lambda 0},z_f)]^{-2/3}} \tag{46}$$

$$= 2.2\ \times\ 10^{-9}\,\frac{c_h^2 c_g^2}{\sqrt{1+c_h^2 c_g^2}}\,(1+z_f)^{3.14}\left(\frac{M_v}{10^{14}\ M_\odot}\right)^{1.16}\,[1+\delta_{coll,non}(\Omega_{m0},\Omega_{\Lambda 0},z_f)]^{2/3}\ h^{-0.17} \tag{47}$$

Now, let's make some approximations to evaluate the above more easily. We take $h = 0.71$; it is known precisely enough, and the dependence on it is weak. We will also take $1+\delta_{coll,non}(\Omega_{m0},\Omega_{\Lambda 0},z_f) = 18\,\pi^2$, its asymptotic value for large z_f. For $z > 0.25$, the deviation from this value is no more than 50%, which gets reduced by the 2/3 power. So we have

$$y_0 = 7.2\ \times\ 10^{-8}\,\frac{c_h^2 c_g^2}{\sqrt{1+c_h^2 c_g^2}}\,(1+z_f)^{3.14}\left(\frac{M_v}{10^{14}\ M_\odot}\right)^{1.16} \tag{48}$$

The signal levels at different important radii are:

$$y_c \equiv y(r_c) = \frac{y_0}{\sqrt{2}} \tag{49}$$

$$= 5.1 \times 10^{-8} \frac{c_h^2 c_g^2}{\sqrt{1 + c_h^2 c_g^2}} (1+z_f)^{3.14} \left(\frac{M_v}{10^{14}\ M_\odot}\right)^{1.16} \tag{50}$$

$$\approx 5.1 \times 10^{-8}\, c_h\, c_g\, (1+z_f)^{3.14} \left(\frac{M_v}{10^{14}\ M_\odot}\right)^{1.16} \tag{51}$$

$$= 5.1 \times 10^{-8}\, h^{-1/5}\, K\, c_g\, \frac{(1+z_f)^{3.14}}{1+z_o} \left(\frac{M_v}{10^{14}\ M_\odot}\right)^{0.96} \tag{52}$$

$$= 1.6 \times 10^{-6}\, \frac{(1+z_f)^{3.14}}{1+z_o} \left(\frac{M_v}{10^{14}\ M_\odot}\right)^{0.96} \tag{53}$$

$$y_v \equiv y(R_v) = \frac{y_0}{\sqrt{1 + c_h^2 c_g^2}} \tag{54}$$

$$= 7.2 \times 10^{-8} \frac{c_h^2 c_g^2}{1 + c_h^2 c_g^2} (1+z_f)^{3.14} \left(\frac{M_v}{10^{14}\ M_\odot}\right)^{1.16} \tag{55}$$

$$\approx 7.2 \times 10^{-8} (1+z_f)^{3.14} \left(\frac{M_v}{10^{14}\ M_\odot}\right)^{1.16} \tag{56}$$

$$y_g \equiv y(r_g) = \frac{y_0}{\sqrt{1 + \sqrt{1 + c_h^2 c_g^2}}} \tag{57}$$

$$= 7.2 \times 10^{-8} \frac{c_h^2 c_g^2}{\sqrt{\left(1 + c_h^2 c_g^2\right)\left(1 + \sqrt{1 + c_h^2 c_g^2}\right)}} (1+z_f)^{3.14} \left(\frac{M_v}{10^{14}\ M_\odot}\right)^{1.16} \tag{58}$$

$$\approx 7.2 \times 10^{-8} \sqrt{c_h\, c_g}\ (1+z_f)^{3.14} \left(\frac{M_v}{10^{14}\ M_\odot}\right)^{1.16} \tag{59}$$

$$= 7.2 \times 10^{-8}\, h^{-1/10} \sqrt{K\, c_g}\ \frac{(1+z_f)^{3.14}}{\sqrt{1+z_o}} \left(\frac{M_v}{10^{14}\ M_\odot}\right)^{1.06} \tag{60}$$

$$= 4.1 \times 10^{-7}\, \frac{(1+z_f)^{3.14}}{\sqrt{1+z_o}} \left(\frac{M_v}{10^{14}\ M_\odot}\right)^{1.06} \tag{61}$$

where we have used $c_g = 5$ and c_h as defined in Equation 8 with $K = 6$ to obtain the final version of each formula. It is important to note the fact, visible in the intermediate results before we have subtituted for c_h and c_g, that the dependence on concentration parameter differs between the three y values: y_v has essentially no dependence on concentration parameters (as long as $c_h\, c_g \gg 1$), y_0 and y_c have linear dependence on the concentration parameters, and y_g has square-root dependence on the concentration parameters. Clearly, predictions of y_v will be most robust against variations in dark matter halo profile and in gas physics. We also summarize the relations between the different y values:

$$y_0 = 32\, \frac{y_v}{1+z_o} \left(\frac{M}{10^{14}\ \mathrm{M}_\odot}\right)^{-1/5} \qquad y_c = \frac{y_0}{\sqrt{2}} \qquad y_g \approx 5.4\, \frac{y_v}{\sqrt{1+z_o}} \left(\frac{M}{10^{14}\ \mathrm{M}_\odot}\right)^{-1/10} \tag{62}$$

We have referenced all values to y_v because y_v is independent of concentration parameters for our normalization method. For the sake of picking a single number to focus on, we take the typical

signal level to be y_g, or

$$\boxed{y_g = 4.1 \times 10^{-7} \frac{(1+z_f)^{3.14}}{\sqrt{1+z_o}} \left(\frac{M_v}{10^{14}\ M_\odot} \right)^{1.06}} \tag{63}$$

This result is similar to those obtained in the literature from theory[11] and from data[12].

2.5 Abundances

As important as signal level and angular size is an estimate of the abundance of detectable objects. The above discussion has shown us how to calculate the observable parameters of a cluster given its mass, formation redshift, and observation redshift. Since we will primarily be interested in observations above some mass threshold, let us consider how the number of clusters depends on the mass cutoff. These abundances are easily calculated using standard Press-Schechter formalism [21], or, more accurately, using simulations [22, 23]. Since the cosmological parameters are sufficiently well defined that there are now essentially no free parameters in these abundances, we simply list the number of clusters per square degree expected above various mass thresholds. Holder *et al.* [24] provide calculations of these abundances based on the simulations in [23]. We use these results to summarize the number of objects in the sky viewable by CCAT [13]:

mass limit	area density	number in 20000 deg^2
$1 \times 10^{14}\,\mathrm{M}_\odot$	40 deg^{-2}	10^6
$3.5 \times 10^{14}\,\mathrm{M}_\odot$	6 deg^{-2}	10^5
$1 \times 10^{15}\,\mathrm{M}_\odot$	0.25 deg^{-2}	few $\times\ 10^3$
$3.5 \times 10^{15}\,\mathrm{M}_\odot$	0.012 deg^{-2}	2×10^2

[11] For example, Bartlett [18] obtains the formula (his Equation 11)

$$y_0(M,z) = (6.40 \times 10^{-5}\, h^2)\, f_{gas}\, \Omega_{m0}\, \frac{\delta_{coll,non}(z)}{18\,\pi^2}\, M_{15}\, (1+z)^3\, \frac{c}{\sqrt{1+c^2}-1}$$

He uses $f_{gas} = 0.06\, h^{-1.5}$. It is not clear whether z refers to formation or observation redshift; we will assume it is z_f. If we make similar approximations to those we have made above, and use $c = c_h c_g$, we obtain $y_0(M,z) \approx 2.8 \times 10^{-6}\, M_{14}^{4/5}\, (1+z_f)^3/(1+z_o)$, which is very close to the y_0 we calculated. Unfortunately, no other authors provide a similar simple form for y_0, so we cannot perform further cross-checks.

[12] Hughes and Birkinshaw [19] and Reese *et al.* [20] find $y_0 = 2.3 \times 10^{-4}$ for CL0016+16 via SZ measurements. Using the Neumann and Bohringer [14] X-ray mass of $2.5 \times 10^{15}\,\mathrm{M}_\odot$ for CL0016+16, our formula predicts $y_0 = 8.8 \times 10^{-5}$ for $z_f = z_o = 0$, low by a factor of 2.6. As we mentioned earlier, the X-ray mass measurement may be an underestimate; and of course, $z_f > 0$ would increase y_0 also. The agreeement is reasonable given these uncertainties.

[13] CCAT can see about 36000 deg^2 above local elevation of 30 deg. We very conservatively assume 20000 deg^2 are sufficiently free of galactic contamination to use. For reference, WMAP discards about 20% of the sky in its full-sky analysis [25].

3 Signal Levels and Angular Scales for Various Objects

With the relations given in Section 2 in hand, we can gauge the signal levels and angular scales of interest.

For reference, we will assume a Gaussian illumination of a 25-m diameter primary with a conservative -10 dB edge taper. The illumination pattern has $\sigma = 5.8$ m and FWHM = 13.7 m. This results in the following beam sizes:

frequency	beam FWHM
275 GHz	0.24 arcmin = 14 arcsec
220 GHz	0.30 arcmin = 18 arcsec
150 GHz	0.44 arcmin = 26 arcsec
100 GHz	0.66 arcmin = 40 arcsec

Given the discussion in the previous section, we will focus our calculations on 150 GHz, but the beam sizes and known frequency dependence of the SZ effects allow one to scale these results to different frequencies.

3.1 Detailed Mapping of Individual Clusters in the Thermal SZ

For the sake of definiteness, we consider clusters at the detection limit of expected blind tSZ surveys such as APEX, ACT, and SPT, which we may like to follow up with CCAT. These surveys will have a detection limit of approximately $2.5 \times 10^{14}\, h^{-1}\ \mathrm{M}_\odot \approx 3.5 \times 10^{14}\ \mathrm{M}_\odot$ [26]. We do not know z_f and z_o, so we conservatively maximize z_o by using $z_o = z_f$ and then also set $z_f = 0$ to minimize the y signal.

- Equation 63 gives signal levels of $y \sim 3 \times 10^{-7}$ and larger at the virial radius ($R_v \approx 2.3$ Mpc, $\theta_v \approx 4.5$ arcmin), corresponding to a temperature signal at 150 GHz of $\Delta T_{\mathrm{CMB}} \sim 0.9\ \mu\mathrm{K}_{\mathrm{CMB}}$. In a 0.44 arcmin FWHM beam at 150 GHz, $y = 3 \times 10^{-7}$ corresponds to a flux density of 6 μJy per beam. Signal levels in cluster cores (y_c) are larger by a factor of as much as 25 ($\Delta T_{\mathrm{CMB}} \sim 20\ \mu\mathrm{K}_{\mathrm{CMB}}$, flux $\sim 140\ \mu$Jy). However, this latter number should be taken with a large grain of salt because, as we have said before, predictions in the core are not robust. Also, observationally, beam dilution will reduce the apparent signal: for the same cluster mass, $r_c \approx 80$ kpc and $\theta_c \approx 0.15$ arcmin, much smaller than the 0.44 arcmin FWHM beam at 150 GHz. The geometric mean radius $r_g \approx 420$ kpc, $\theta_g \approx 0.83$ arcmin, is a much better match to the beam size, and we expect $y_g \approx 1.8 \times 10^{-6}$ ($\Delta T_{\mathrm{CMB}} \sim 5\ \mu\mathrm{K}_{\mathrm{CMB}}$, flux $\approx 35\ \mu$Jy).
- Equations 19, 21, and 23 imply that we need information on angular scales (diameter) from roughly 0.1 arcmin to 10 arcmin. The beam obviously provides a lower limit that is greater than 0.1 arcmin, but the 10 arcmin criterion points to the necessary field of view.

Confusion from infrared and radio points sources is an issue at these signal levels; confusion will be discussed later.

3.2 Kinetic SZ in Individual Clusters

The kinetic SZ effect depends on both the optical depth of the cluster and its line-of-sight peculiar velocity. Peel [27] finds by simulation the peculiar velocity distribution for cluster-size halos. It is generically found that the 1-dimensional, 2-dimensional, and 3-dimensional RMS velocities are 311 km s^{-1}, 440 km s^{-1}, and 539 km s^{-1}, with no apparent dependence on cluster mass. Thus, $v/c \approx 10^{-3}$ to good accuracy.

For a cluster at the detection limit of the large-area tSZ surveys, $M \approx 3.5 \times 10^{14}$ $M_\odot$, we obtain from Equation 31 a central optical depth of 1.8×10^{-3}. Since we saw earlier that the cluster core is very small compared to our beam, let us instead consider the signal level at $\theta_g \approx 0.83$ arcmin for such a cluster. The optical depth drops by a factor of roughly 5.4 (same as for y_g/y_0) to $\tau(r_g) \approx 3.6 \times 10^{-4}$. Assuming the aforementioned v/c of 10^{-3}, we obtain $\Delta T_{\rm CMB}/T_{\rm CMB} = 4 \times 10^{-7}$, $\Delta T_{\rm CMB} = 1$ $\mu{\rm K}_{\rm CMB}$, and a flux density of 8 μJy.[14] Because of the weak dependence on cluster mass, larger clusters will not yield much larger signals unless they have enhanced baryon fraction or concentration. At any signal size, confusion from point sources will again be an issue, to be addressed later in this document.

3.3 Blind tSZ Surveys for Low-Mass Objects

The large-area blind tSZ survey such as APEX-SZ, ACT, and SPT will have a limiting mass of about 3.5×10^{14} $M_\odot$. Blind tSZ surveys have been studied extensively [28, 26, 18, 12, 29, 30, 31]; one general conclusion is that the optimal depth for a survey is that at which the lowest-mass clusters detected match the beam size. Thus, it might be sensible to conduct a survey to lower mass with CCAT given its significantly better angular resolution. As an exercise, let us calculate the angular sizes and integrated flux densities for objects of mass 10^{12} $M_\odot$, 10^{13} $M_\odot$, and 10^{14} $M_\odot$. The relation for $Y_{\rm Mpc^2}$ from da Silva *et al.*used before is known to be valid down to 10^{13} $M_\odot$; we will blindly extrapolate it down to 10^{12} $M_\odot$. Let us use Equation 38 for S_ν and Equation 40 for $Y_{\rm Mpc^2}$, and specialize to $\nu = 150$ GHz:

$$S_\nu = B_\nu(x)\, h(x)\, f(x)\, \frac{1}{d_A^2(z_o)} 10^{-6}\, (1+z_f)^{1.14} \left(\frac{M_v}{10^{14}\ M_\odot}\right)^{1.83} h^{-0.17}\ {\rm Mpc}^2 \tag{64}$$

$$= \left(\frac{1}{c/H_0}\right)^2 h^{-0.17} B_\nu(x)\, h(x)\, f(x)\, \left(\frac{c/H_0}{d_A(z_o)}\right)^2 10^{-6}\, (1+z_f)^{1.14} \left(\frac{M_v}{10^{14}\ M_\odot}\right)^{1.83}\ {\rm Mpc}^2 \tag{65}$$

$$= 60 \left(\frac{c/H_0}{d_A(z_o)}\right)^2 (1+z_f)^{1.14} \left(\frac{M_v}{10^{14}\ M_\odot}\right)^{1.83}\ \mu{\rm Jy} \tag{66}$$

As a check, we note that the 3.5×10^{14} $M_\odot$ mass limit of the large-area blind surveys corresponds to about 6 mJy. This value is consistent (to a factor of 2) with Table 1 of the Battye, *et al.* [30] tSZ survey optimization paper.

For the objects of the specified masses, conservatively taking $z_f = 0$ and the angular diameter distance factor to be 2.5^2, we have (using Equation 21 for θ_s):

mass	flux density	θ_s
10^{12} $M_\odot$	0.08 μJy	0.02 arcmin
10^{13} $M_\odot$	5 μJy	0.05 arcmin
10^{14} $M_\odot$	350 μJy	0.1 arcmin

Note the fast decrease of flux density with mass. The mass-dependence of the flux density is so strong because the flux density depends on both mass and temperature; the latter goes as M^α, $\alpha = 2/3$ to 1. One may get a mild enhancement from the fact that lower-mass objects form earlier

[14] The fact that this kSZ flux estimate is only a factor of 4 – 5 smaller than the tSZ flux estimate at the same radius made in Section 3.1 is no doubt surprising, but it can be explained by simply noting that the estimate is being made for fairly low-mass clusters. One is used to seeing such estimates for 10^{15} $M_\odot$ clusters. The tSZ signal increases much more quickly with mass than the kSZ signal because of the former's temperature dependence. This gives a factor of 3 difference between tSZ and kSZ. The ratio of the two signals becomes roughly 10, which is probably what the reader expects.

and thus z_f can be as large as 5 to 10, which may allow detection of 10^{13} $M_\odot$ objects, but 10^{12} $M_\odot$ objects are definitely out of reach.

3.4 Primary CMB Anisotropy

Primary CMB anisotropy suffers an exponential dropoff in amplitude for angular multipole number $\ell > 2000$ ($\lambda_\theta < 10.8$ arcmin where λ_θ is the angular wavelength of the mode) due to photon diffusion at the surface of last scattering (Silk damping). Thermal SZ anisotropy (Section 3.5) is expected to match primary CMB anisotropy in amplitude at $\ell \approx 2000 - 4000$ (see for example, [7], though any of the references listed in Section 3.5 will suffice). This is not damning because tSZ is spectrally distinguishable. Spectrally indistinguishable kSZ anisotropy (see Section 3.5) is expected to dominate over primary anisotropy for $\ell > 4000$. If we assume a field of view of 20 arcmin, it is plausible that some primary anisotropy could be detected.

There are two arguments against focusing on primary anisotropy, though. Sky subtraction will make it difficult to see such FOV-size structure, though perhaps less aggressive sky subtraction (or none at all) could be used to recover the exponentially rising signal. But, perhaps more importantly, there are a number of other experiments – APEX, ACT, and SPT – that will be better optimized for detection of such signals and will take data much sooner. We thus do not include primary CMB anisotropy as an important science goal for CCAT.

3.5 Distributed SZ Anisotropy Power Spectra

While we have so far discussed detection of SZ effects in individual clusters, one may also consider trying to detect the distributed anisotropy due to the accumulated SZ fluctuations between today and the surface of last scattering. The mean comptonization is not easily detectable because it requires an absolute measurement, but fluctuations are accessible.

Many authors have calculated tSZ and kSZ[15] anisotropy power spectra [32, 33, 34, 35, 36, 7, 37, 38]. At 150 GHz, these signals typically have approximately flat bandpowers of about 10 μK^2_{CMB} (at 150 GHz – the tSZ temperature fluctuation is frequency-dependent) and 1 μK^2_{CMB} (kSZ) in the angular multipole range $\ell \sim 1000 - 20000$, with variations of a factor of a few in these predictions depending on the assumptions going into the calculation. No one has done serious predictions for $\ell > 10000$, but it is expected that the signal has a wide peak in ℓ-space at $\ell \sim 5000 - 10000$; there is, for example, no expected exponential fall-off as with primary anisotropy.

The expected variance due to SZ anisotropy in map-space is obtained by multiplying the expected bandpower ($C_l\, \ell\, (\ell + 1)\, /2\, \pi$, in μK^2_{CMB}) against the logarithmic ℓ-space bandwidth, $\Delta \log \ell$. Assuming a CCAT SZ instrument is sensitive on length scales from the beam size ($\sigma \approx 0.2$ arcmin at 150 GHz) to the field of view (≈ 20 arcmin), the latter factor is $\Delta \log \ell \approx 4.6$, so we expect rms map-space signals of 7 μK_{CMB} for tSZ at 150 GHz and 2 μK_{CMB} for kSZ. Distributed kSZ is surprisingly large compared to distributed tSZ, presumably because it is not so strongly mass-dependent; though kSZ does suffer an additional line-of-sight cancellation.

Another effect, termed "patchy reionization", occurs because the ionization fraction of the baryons is modulated by reionization – regions around large sources of UV photons are more ionized than the IGM in general. One can obtain a kSZ effect from these regions. The anisotropy

[15] On the Ostriker-Vishniac effect: the distinction between kSZ and OV effects is purely semantic. kSZ usually refers to the effect in the nonlinear regime while OV usually refers to the linear fluctuation regime. They are the same underlying physics. Note that, to first order, any kSZ fluctuation disappears because any fluctuation on the line of sight with one sign of velocity with have a corresponding fluctuation with the opposite sign. When viewed this way, kSZ occurs because nonlinear collapse ruins the cancellation and OV occurs due to second-order correlations between the linear density and velocity fields. We shall subsume OV into kSZ for all our discussions.

signal levels are a factor of a few smaller than the standard kSZ mentioned above. We will neglect patchy reionization.

3.6 Primary CMB Polarization Anisotropy

As with primary temperature anisotropy, primary polarization anisotropy falls off exponentially at high ℓ due to Silk damping. For the same reasons as above, we therefore do not consider it.

3.7 Polarized SZ in Individual Clusters

Polarized SZ effects arise in the same manner as primary CMB polarization anisotropy – if a free electron sees a radiation field with a quadrupole anisotropy, then the scattered radiation exhibits a polarization related to that anistropy. Such quadrupole anisotropy occurs in three ways: intrinsic quadrupole anisotropy in the radiation field incident on the cluster; quadrupole anisotropy engendered as a result of the peculiar motion of the cluster (second-order in v/c); and quadrupole anisotropy created by double-scattering of CMB photons in a single cluster (a τ^2 effect). The first effect is by far the most important because it provides multiple measurements of the CMB quadrupole anisotropy from independent last-scattering surfaces, allowing one to beat cosmic variance. Given the significant suppression of large-scale CMB anisotropy as compared to predictions [25], this could be a very important measurement.

In calculating signal levels, we first note that these effects are thermal in that they result in thermodynamic temperature changes of the CMB; they do not Comptonize the CMB as the tSZ effect does. So we may speak of $\Delta T_{\rm CMB}/T_{\rm CMB}$ signals without ambiguity. The expected signal levels are:

- Intrinsic quadrupole anisotropy: As first calculated by Zeldovich and Sunyaev [39], this signal has $\Delta T_{\rm CMB}/T_{\rm CMB} = 0.1\,\tau\,Q$ where Q is the intrinsic quadrupole anisotropy in $\Delta T_{\rm CMB}/T_{\rm CMB}$, $Q \approx 6 \times 10^{-6}$ as measured by COBE [40]. For $\tau = 10^{-3} - 10^{-2}$ (reasonable levels for massive clusters as explained in Section 3.2), we have $\Delta T_{\rm CMB}/T_{\rm CMB} \approx 6 \times 10^{-10} - 6 \times 10^{-9}$, or $\Delta T_{\rm CMB} = 1.5 - 15$ nK$_{\rm CMB}$.

- Velocity-induced quadrupole anistropy. This effect was first calculated by Sunyaev and Zeldovich [41] and has size $\Delta T_{\rm CMB}/T_{\rm CMB} = 0.1\,(v_\perp/c)^2\,\tau$, where $v_\perp$ is the velocity transverse to the line of sight. Using the 2D velocity dispersion of 440 km s^{-1} calculated above, and $\tau = 10^{-3} - 10^{-2}$, we obtain $\Delta T_{\rm CMB} = 0.2 - 2$ nK$_{\rm CMB}$.

- Double-scattering induced quadrupole anisotropy. This effect was also first noted by Sunyaev and Zeldovich [41] and is of size $\Delta T_{\rm CMB}/T_{\rm CMB} = 0.025\,(v_\perp/c)\,\tau^2$, so the signal level is $\Delta T_{\rm CMB} = 0.03 - 3$ nK$_{\rm CMB}$.

These signals are clearly very small. The saving grace is that they are polarized. This will, first of all, greatly mitigate the effect of sky noise in degrading instrument sensitivity. But it is certainly expected that radio point sources, and possibly infrared point sources, will show low-level polarization, so we cannot be guaranteed of polarization-free confusion noise. Further discussion will be provided later.

3.8 Distributed Polarized SZ Anisotropy

Hu [36] calculates the power spectrum of polarization anistropy due to distributed effects of the same kind discussed in Section 3.7. These effects are at the few nK$_{\rm CMB}$ level and below. Since we

will see later that even polarized SZ in clusters is essentially undetectable, we do not discuss this small signal further.

4 Expected Sensitivities and Integration Times

4.1 Continuum Observations

Given the signal levels predicted above, how realistic is it to do these SZ observations? A first-order answer can be obtained by simply comparing the signal levels to the expected background-limited sensitivity. We assume we are in the Rayleigh-Jeans limit of the background optical load. The background-limited sensitivity is therefore

$$\mathrm{NET_{RJ}} = \frac{\mathrm{NEP}/\sqrt{2}}{2\,k\,\eta\,\Delta\nu} \tag{67}$$

$$= \frac{1}{2\sqrt{2}\,k\,\eta\,\Delta\nu}\left[2\,Q\,h\,\nu + \frac{Q^2}{\Delta\nu}\right]^{1/2} \tag{68}$$

$$= \frac{1}{2\sqrt{2}\,k\,\eta\,\Delta\nu}\left[4\,k\,T\,\eta\,\Delta\,\nu\,h\,\nu + 4\,k^2\,T^2\,\eta^2\,\Delta\,\nu\right]^{1/2} \tag{69}$$

$$= \sqrt{\frac{T\,(h\,\nu + k\,T\,\eta)}{2\,k\,\eta\,\Delta\nu}} \tag{70}$$

where T is the total optical loading in Kelvins, ν is the central frequency, $\Delta\nu$ is the bandwidth, and η is the overall optical efficiency. The division of NEP by $\sqrt{2}$ is the usual conversion from $\mathrm{Hz}^{-1/2}$ to $\mathrm{s}^{1/2}$. Numerically, we have

frequency (GHz)	atmosph. transm.	$\mathrm{NET_{RJ}}$ ($\mu\mathrm{K_{RJ}\ s^{1/2}}$)	$\mathrm{NET_{CMB}}$ ($\mu\mathrm{K_{CMB}\ s^{1/2}}$)	NEFD (mJy $\mathrm{s^{1/2}}$)
100	0.93	210	270	2.7
150	0.93	180	310	2.3
220	0.905	170	530	2.2
275	0.86	190	1000	2.5

We have used $\Delta\nu/\nu = 0.3$, $T = 45$ K, and $\eta = 0.5$. T assumes 10% telescope emissivity at 273 K, opacities at 1.5 mm PWV, $T_{atm} = 273$ K, and zenith angle of 30 deg; all from T. Herter's sensitivity worksheet.

Terry's spreadsheet gives a sensitivity at 150 GHz of 2.3 mJy $\mathrm{s^{1/2}}$, which includes a $\sqrt{2}$ degradation for chopping. Terry's calculation uses a smaller beam (22 arcsec) thanks to a more aggressive edge taper; adjusting the edge taper of our primary illumination to 7 dB instead of 10 dB would reduce the above NEFD to 1.6 mJy $\mathrm{s^{1/2}}$, which would then match Terry's number when the $\sqrt{2}$ degradation is applied. For calculations, we use the 2.3 mJy $\mathrm{s^{1/2}}$ number (and its equivalents in other units and at other frequencies).

If we naively assume that a cluster is covered by the focal plane so that instantaneously one always obtains the above sensitivity over the entire cluster, then reaching $1\,\mu\mathrm{K_{CMB}}$ rms at 150 GHz requires 96 ksec, or about 7 eight-hour nights at 50% observing inefficiency. The sensitivity is really too poor to try to map thermal SZ at high S/N in the virial wings of a $3.5 \times 10^{14}\,\mathrm{M_\odot}$ cluster (signal level $\sim 1\,\mu\mathrm{K_{CMB}}$). Azimuthally averaged radial profiles should be accessible in reasonable amounts of time, and mapping should be possible for higher mass clusters.

It is important to note that the sensitivity at these frequencies is largely limited by telescope emissivity! Reducing the telescope emissivity to 5% and keeping all other parameters fixed would improve the sensitivity at 150 GHz to 230 μK_{CMB} $s^{1/2}$ and would reduce the necessary integration time by almost half to 260 ksec. Using a more reasonable $T_{atm} = 250$ K further reduces these values to 220 μK_{CMB} $s^{1/2}$ and 240 ksec, and taking data in 1 mm PWV weather would further bring them down to 190 μK_{CMB} $s^{1/2}$ and 180 ksec, or about 12 nights. Clearly, the dominant effect is the telescope emissivity. At 275 GHz, one gets about equal $\sqrt{2}$ improvements in sensitivity from reducing the telescope emissivity by a factor of 2 to 5% or by reducing the atmospheric opacity by a factor of 2 to 7%.

It should be noted that the ACBAR receiver on the Viper telescope (an off-axis Gregorian with a chopping tertiary) at the South Pole measures a telescope emissivity of only 1.5% with a 3-mirror design at 150 GHz. This is actually 3 times the theoretical value, presumably due to mirror roughness. Mirror roughness at 150 GHz for the CCAT should really be non-issue, and we expect to need only one additional reflective optical element prior to entering the dewar (unless flat mirrors are needed to fold the beam), so achieving 5% emissivity seems feasible as long as care is taken in the optical design at all steps. Other critical contributors will be feed-leg blockage and diffraction, cracks between the panels, and reflection from the center of the secondary. These problems can be addressed by minimization of feed-leg mass and possibly arching the legs so they are only seen once by the beam, careful matching of panel edges (presumably important at the highest frequencies also), and opening a hole in or providing an oblique scattering cone at the secondary.

Detection of polarized SZ effects seems unlikely to be successful – even assuming the most optimistic sensitivities above, reaching signal levels of order 10 nK_{CMB} would take $\sim 10^9$ sec.

4.2 Spectroscopic Observations

Low-resolution spectroscopy of the tSZ effect could be as useful as spatially-resolved observations in understanding cluster astrophysics as well as in gauging and removing confusion. Resolution of about 3 GHz would be sufficient ($R \sim 30-100$) to see the broadband spectral signatures of thermal and kinetic SZ, to directly see relativistic effects, and to probe for contamination by point sources.

By way of explanation: Corrections to the tSZ effect due to relativistic motion of the scattering electrons provide sensitivity to the gas temperature. The first relativistic calculation of the tSZ spectrum was performed by Rephaeli [42]; there have been further refinements since [43, 44, 45, 46, 47, 48, 49, 50, 51]. Low-resolution spectra taken at various locations and covering the frequency range from 100 GHz to 300 GHz would be useful in measuring spatially resolved temperature profiles. The deviation from the nonrelativistic spectrum is of course frequency- and T_e-dependent. At the increment-side peak, the effect is roughly 20% for $T_e = 15$ keV, 10% for $T_e = 10$ keV, and between 5% and 10% at $T_e = 5$ keV.

We have already calculated flux density levels for the nonrelativistic SZ effects, so we simply need to determine whether observations over the restricted bandwidth of a spectrometer channel are sufficiently sensitive to see these signals. As we did above, we assume we are in the Rayleigh-Jeans

limit for the optical loading. The background-limited flux sensitivity is therefore

$$\mathrm{NEF} = 2\sqrt{2}\,\frac{\mathrm{NEP}/\sqrt{2}}{A\,\eta} \tag{71}$$

$$= \frac{2}{A\,\eta}\left[2\,Q\,h\,\nu + 2\,\frac{Q^2}{\Delta\nu}\right]^{1/2} \tag{72}$$

$$= \frac{2\,\Omega_b}{\eta\,\lambda^2}\left[2\,k\,T\,\eta\,\Delta\nu\,h\,\nu + 2\,k^2\,T^2\,\eta^2\,\Delta\nu\right]^{1/2} \tag{73}$$

$$= \frac{4\,\pi\,\sqrt{2}\left(\frac{\mathrm{FWHM}}{2\sqrt{2\,\log 2}}\right)^2}{\eta\,\lambda^2}\left[k\,T\,\eta\,\Delta\nu\,(h\,\nu + k\,T\,\eta)\right]^{1/2} \tag{74}$$

where we have used the throughput theorem ($A\,\Omega_b = \lambda^2$). The prefactors of 2 and $\sqrt{2}$ are due to the need to chop and referring back to an unpolarized source (the waveguide spectrometer works in only one polarization). The calculation of the NEP differs by a couple factors from the analogous calculation for continuum sensitivity. First, the Bose term picks up an extra factor of 2 because all the power comes in one polarization. Second, the relation between T and Q loses a factor of 2 because only one polarization is observed. Note also the units – it is standard to discuss spectroscopic sensitivities in terms of flux, not flux density. Numerically, we have

frequency (GHz)	atmosph. transm.	NEF W m^{-2} s$^{1/2}$
100	0.93	5.1×10^{-19}
150	0.93	5.3×10^{-19}
220	0.905	6.3×10^{-19}
275	0.86	7.8×10^{-19}

We have used $\Delta\nu = 3$ GHz, $T = 45$ K, and $\eta = 0.5$. T assumes 10% telescope emissivity at 273 K, opacities at 1.5 mm PWV, $T_{atm} = 273$ K, and zenith angle of 30 deg; all from T. Herter's sensitivity worksheet. The sensitivities calculated above are within a factor of $\sqrt{2}$ of those calculated in Terry's worksheet.

For the lowest-mass clusters of interest for detailed follow-up, at 3.5×10^{14} $M_\odot$, we calculated that the tSZ flux density at 150 GHz in the virial wings is about 6 μJy per beam, or 1.8×10^{-22} W m^{-2} in a 3 GHz spectroscopic channel. Detecting this signal at 5σ would require an integration time of 4.3×10^7 sec, clearly unfeasible. Larger signals are easily available, though:

- In cluster cores, the tSZ signal should be about a factor of 30 higher.
- y is a slightly faster than linear function of mass (Equation 63), so study of higher mass clusters will be possible – each factor of ~ 3 in mass would decrease the necessary integration time by ~ 10.

A $10^{15}\,M_\odot$ cluster could be observed in the core in < 100 ksec and a 3.5×10^{15} $M_\odot$ cluster in the core in < 5 ksec and in the virial wings in 20 ksec. These massive clusters are the ones for which the relativistic effects will be most important, so they are actually the most interesting clusters to study spectroscopically.

From the instrumental point of view, note that a background-limited spectrometer with higher R ($\sim 300 - 1000$ has been discussed) would have poorer sensitivity per channel, but channels could be coadded at no loss to obtain degraded resolution and better sensitivity (assuming each channel is background-limited). However, the instrument becomes proportionally larger as the resolving

power is increased; a major advantage of a $R \sim 30-100$ instrument would be its compactness. The only reason to build a higher-resolution spectrometer would be if there are interesting line searches to be done in the 100 – 300 GHz range.

5 Confusion Noise

Clearly, a significant issue for these measurements will be confusion noise. Possible sources to consider:

- Extragalactic infrared point sources
- Galactic cirrus
- Extragalactic radio point sources
- Galactic synchrotron and free-free
- CMB primary anisotropy

We list here current estimates for these confusion signal levels and discuss how they might be dealt with.

5.1 Infrared Sources

Diffuse galactic cirrus emission will yield fluctuations smaller than those due to extragalactic point sources [52, 53], so we neglect cirrus confusion.

A. Blain has calculated confusion levels from infrared sources [52]. Given the conservative edge taper we have assumed, we cannot use his calculations for a 25-m diameter telescope. Rather, we find the telescope diameter whose beam sizes matche the ones we obtain with our conservative edge taper. This turns out to be about 20-m telescope, so we simply use his calculations for a 20-m telescope. The 1 source per beam confusion levels are:

frequency	flux density	temperature	y parameter
275 GHz	66 μJy	27 μK_{CMB}	1.1×10^{-5}
220 GHz	89 μJy	21 μK_{CMB}	N/A
150 GHz	44 μJy	6 μK_{CMB}	2.3×10^{-6}
100 GHz	21 μJy	2.1 μK_{CMB}	5.1×10^{-7}

One obvious conclusion is that 100 GHz is really the best place to work vis-a-vis infrared-source confusion. However, 100 GHz will be covered by the SZA high-frequency channel, so it's not a unique application.

Focusing momentarily on 150 GHz, the confusion limit is a factor of a few higher than the tSZ effects we would like to observe in the lowest-mass clusters accessible by the blind large-area surveys (3.5×10^{14} $M_\odot$). Is removal of infrared point sources using higher-frequency or higher-angular-resolution maps possible?

5.1.1 Cleaning of tSZ Maps using Higher-Frequency CCAT Maps

Let us scale the above confusion limits to 350 GHz and 490 GHz and estimate how much CCAT time would be needed to detect these point sources at 5σ at these frequencies. It is reasonable to assume the 350 GHz camera will cover the same FOV as the SZ camera – $f\,\lambda$ at 350 GHz is roughly

10 arcsec, so a 20 arcmin field of view is covered by 3600 pixels at $2\,f\,\lambda$ and 14400 pixels at $0.5\,f\,\lambda$. At 490 GHz, the number of pixels needed to fill the same field of view increases by about 2. We adopt sensitivities of 5.8 mJy $s^{1/2}$ and 16.4 mJy $s^{1/2}$ for 350 GHz and 490 GHz respectively.[16] We scale the 350 GHz and 490 GHz sensitivities to the band of interest using a $\nu^{3.7}$ spectrum (typical for dust emission, especially at these low frequencies). The resulting sensitivities and time needed to obtain 5σ detections of sources at the confusion limit over the field of view are

	350 GHz		490 GHz	
frequency	NEFD	T for FOV	NEFD	T for FOV
275 GHz	2400 μJy $s^{1/2}$	32000 sec	1900 μJy $s^{1/2}$	21000 sec
220 GHz	1000 μJy $s^{1/2}$	3400 sec	850 μJy $s^{1/2}$	2300 sec
150 GHz	250 μJy $s^{1/2}$	820 sec	210 μJy $s^{1/2}$	540 sec
100 GHz	56 μJy $s^{1/2}$	180 sec	46 μJy $s^{1/2}$	120 sec

So, sources at the 1 source per beam confusion limit can be observed at 350 GHz and 490 GHz in a very reasonable amount of time.

The above table does not tell the whole story, though. In order to identify and remove a source from a low-frequency map, one must have a solid detection and flux for the source in the high-frequency maps. Therefore, the high-frequency maps must be no deeper than roughly the 1 source per 30 beams, or maybe 1 source per 10 beams, confusion level. These confusion levels are 830 μJy and 390 μJy at 350 GHz and 1200 μJy and 500 μJy at 490 GHz, respectively. Let us extrapolate these confusion limits to the SZ bands, again assuming a $\nu^{3.7}$ spectrum:

	350 GHz		490 GHz	
	1 src per	1 src per	1 src per	1 src per
frequency	30 beams	10 beams	30 beams	10 beams
275 GHz	340 μJy	160 μJy	140 μJy	59 μJy
220 GHz	150 μJy	70 μJy	62 μJy	26 μJy
150 GHz	36 μJy	17 μJy	15 μJy	6.3 μJy
100 GHz	8.1 μJy	3.8 μJy	3.4 μJy	1.4 μJy

Clearly, the sensible thing to do is to remove the brighter sources using the 350 GHz data (so the spectral index extrapolation systematic error is minimized) and remove the dimmest sources using the 490 GHz data (where the systematic subtraction error will be dominated by the high-frequency flux error). Removal of sources to a factor of 3 below the 1 source per beam limit is plausible in the 100 and 150 GHz bands. The infrared source counts are steeper than S^{-2}, so a factor of 3 in flux gives on factor of at least 9 in source density, so it is plausible that one can push the density of sources down to 1 per 10 beams at 44 μJy at 150 GHz, low enough to secure reasonable detections of 3.5×10^{14} $M_\odot$ clusters at θ_g. We can get to roughly the 1 source per beam limit at 220 GHz and a factor of 2 above the 1 source per beam limit at 275 GHz.

We would like to go deeper, though – getting down to the 1 source per beam limit prevents us from studying the virial wings of the least massive clusters. Much of the cluster mass will be in these wings, so precise study of them would be useful. It may be possible to go deeper by abandoning one-by-one identification and subtraction of sources. Suppose one integrates down so far at 350 GHz and 490 GHz to become totally confused. One can still use this map to do removal at other frequencies because identification of individual sources is not important here. One can simply regress the high-frequency maps against the 150 GHz map. At large fluxes, variations in

[16] The sensitivities number is taken from T. Herter's spreadsheet (2005/03/25 version) and assumes 1 mm PWV for 350 GHz and 0.7 mm PWV for 490 GHz, 30 deg zenith angle, $\sqrt{2}$ sky removal loss, etc.

SED from source to source might be a problem, but these sources can be identified and removed one-by-one. Once one gets down to roughly the 150 GHz confusion limit, the sources merge and one just gets some average SED of the entire population. This averaging ensures that a single regression coefficient will serve to remove the high-frequency point sources from the 150 GHz map. This kind of analysis is planned for ACT [38].

It becomes clear that one can directly remove sources down to $y \approx 2.3 \times 10^{-6}$ at 150 GHz, which comparable to the expected y value at θ_g in a $3.5 \times 10^{14}\,\mathrm{M}_\odot$ cluster. Using the aforementioned regression technique, removal of sources to a factor of a few lower flux should be possible. Thus, it is likely that we will be able to obtain some information about the virial wings of $3.5 \times 10^{14}\,\mathrm{M}_\odot$ clusters and will be able to study in detail $10^{15}\,\mathrm{M}_\odot$ clusters.

5.1.2 Cleaning of tSZ Maps using In-Band ALMA Maps

We may also ask whether observations with ALMA in the band of interest would permit direct removal of sources (as opposed to to extrapolation from another band assuming a SED). We use the ALMA integration time calculator [54].[17] We find sensitivities, FOV, and inferred total time needed to map 100 arcmin^2 to the aforementioned confusion limits (ALMA 5σ = CCAT in-band 1-source-per-beam confusion limit):

frequency	NEFD	FOV	T for 100 arcmin^2
275 GHz	920 μJy s$^{1/2}$	0.10 arcmin^2	5×10^6 sec
220 GHz	730 μJy s$^{1/2}$	0.15 arcmin^2	1.1×10^6 sec
150 GHz	490 μJy s$^{1/2}$	0.33 arcmin^2	1×10^6 sec
100 GHz	320 μJy s$^{1/2}$	0.74 arcmin^2	8×10^5 sec

ALMA is thus not usable for obtaining in-band measurements for confusion removal over large fields. This difficulty results from ALMA's small field of view.

ALMA follow-up is useful in two limits:

- When removing the brightest in-band sources, extremely precise flux, position, and shape knowledge are necessary to avoid systemic subtraction errors in the wings of the beam. Using CCAT 350 GHz observations and extrapolating will result in systematic errors proportional to the flux of the source being subtracted. So subtraction will be most problematic for the brightest sources. But ALMA can be used to obtain in-band – not extrapolated – information for these brightest sources. In 100 times less integration time than given above, an entire 100 arcmin^2 field could be covered by ALMA to 2% precision at 100 times the confusion limit and 20% precision at the confusion limit. Perhaps integration times could be reduced further by using the CCAT 150 GHz map to identify bright source candidates and following only these up with ALMA (though, one has to worry more about bias in using the CCAT in-band map to select sources for follow-up).

- In some cases – studying core substructure, for example – one is interested only in the cluster core (out to θ_g), so one would require removal of infrared sources over only 10–20 arcmin^2, reducing the ALMA time needed to a reasonable amount at 150 GHz. At higher frequencies, removing sources down to the confusion limit does not help with tSZ: at 275 GHz, the confusion limit is a factor of 5 higher in y than at 150 GHz, and, at 220 GHz, one has no sensitivity to tSZ. Thus, one can probe tSZ substructure at 150 GHz, but not at higher frequencies.

[17] The calculator is not available for the 150 GHz band, we interpolate between the 100 GHz and 220 GHz sensitivities.

5.1.3 Cleaning of kSZ Maps

Kinetic SZ has a much weaker mass dependence. The expected flux density for a 3.5×10^{14} $M_\odot$ cluster at θ_g was shown earlier (Section 3.2) to be about 8 μJy per beam (1 μK_{CMB}) at 150 GHz. Note that using such low-mass clusters for the estimate is not unduly pessimistic; since the kSZ signal scales only as $M^{2/15}$, one would gain only a factor of 1.4 in signal for a cluster mass a factor of 10 larger.

This signal level is about a factor 5 – 6 below the confusion limit at 150 GHz. As explained above, explicit source removal will let us reach roughly this noise level, and it is possible that cross-correlation of 350 GHz and lower-frequency maps will permit removal to the necessary levels to detect kSZ with some signal-to-noise.

One must achieve similar sensitivities at 220 GHz and 275 GHz, though, in order to demonstrate the appropriate spectral signature for kSZ. Removal of confusion at these higher frequencies is much more difficult because: 1) a given rms in μK_{CMB} corresponds to smaller flux at higher frequency; and 2) infrared point sources are brighter at higher frequencies, so confusion occurs at a much higher flux. One thing that makes subtraction easier is that one needs to achieve the same μK_{CMB} sensitivity at the higher-frequency bands on pixels the size of the 150 GHz beam, not on pixels matching the beam sizes at 220 GHz and 275 GHz, so the sensitivity requirement is relaxed by about a factor of 1.5 at 220 GHz and 1.8 at 275 GHz relative to 150 GHz. The result is that the flux per beam sensitivity that must be achieved at the three frequencies is almost the same; for example, 1 μK_{CMB} corresponds to 7.5 μJy at 150 GHz and requires 1.5 μK_{CMB} (9 μJy) at 220 GHz and 1.8 μK_{CMB} (8 μJy) at 275 GHz.

Removal of sources at 220 GHz and 275 GHz using 350 GHz or 490 GHz data cannot reach these flux levels. ALMA obtains 1σ sensitivity over one field of view (0.15 arcmin^2 and 0.10 arcmin^2) matching these flux levels in 6.6 ksec and 13 ksec at 220 GHz and 275 GHz, respectively. Observing and removing confused sources over a 1 arcmin^2 cluster core is feasible, but covering much more area – *e.g.*, 10 arcmin^2 for the core of a massive cluster – requires inordinate integration times.

Obtaining high signal-to-noise kSZ maps is thus not possible, even at θ_g. However, what about a lower signal-to-noise detection obtained by integrating over the entire cluster core? This is not very interesting to pursue because it will essentially be done by ACT and SPT. If we degrade our subtraction requirements so that we obtain $S/N = 1$ on the kSZ in each map pixel, we detect kSZ at reasonable S/N by coadding map pixels, at the cost of degraded angular resolution. Degradation by a factor of 2.5 yields the same beam size as SPT, degradation by a factor of 4 matches ACT's beam size, so we obtain no new information.

However, pursuing a similar approach – aiming for $S/N = 1$ per beam – for kSZ anisotropy does probe the level of kSZ anisotropy at angular scales smaller than those accessible by ACT or SPT. This is possible because the level of anisotropy is (statistically) the same at all points in the field of view, so one obtains multiple measurements, allowing a high S/N detection without degrading angular resolution by coadding pixels. Unfortunately, the confusion removal needed to do even a low per-beam S/N measurement is unattainable. To obtain $S/N = 1$ for 2 μK_{CMB} rms kSZ anisotropy, one needs to obtain 3.7 μK_{CMB} in a 275 GHz beam to provide 2 μK_{CMB} when smoothing to the 150 GHz beam. This corresponds to 9 μJy per beam. ALMA would require 12 Msec to map an entire 100 arcmin^2 field to this depth (1σ).

One is prompted to wonder – how is it that CCAT, with its better angular resolution than ACT, will have such trouble in detecting kSZ when ACT expects to measure the kSZ anisotropy power spectrum? Because CCAT has better angular resolution and the infrared source counts are steeper than Euclidean. Were the counts Euclidean, the confusion limit would scale up in flux with the beam area as the telescope size decreases, corresponding to a confusion limit fixed in temperature

(surface brightness) units. But, since the counts fall off more quickly than Euclidean, the confusion limit in flux units does not increase as quickly as the beam size, or, equivalently, the confusion limit in temperature units decreases as the beam size increases. Ironic.

5.1.4 Use of Low-Resolution Spectroscopy

Low-resolution spectroscopy may be usable to set limits on confusion. As we demonstrated in Section 4.2, low-resolution spectroscopy should be possible for 10^{15} $M_\odot$ clusters. We will likely try to observe the kSZ in these fairly high mass clusters first because of their higher electron optical depth, the higher signal level in the tSZ, and the availability of X-ray observations. Some detailed simulation work is needed to determine how useful spectroscopy can be in separating kSZ from infrared sources.

5.2 Radio Sources

Toffolatti *et al.* [55] calculate confusion limits using revisions of various previous galaxy formation models. Their calculations can be easily extrapolated to the angular scales of interest here. We simply continue the curves given in Figure 4 of their paper as power laws. These give the following radio point source confusion limits (again, 1 source per beam):

frequency	flux density	temperature
275 GHz	$\ll 1\,\mu$Jy	$\ll 0.4\,\mu\mathrm{K_{CMB}}$
215 GHz	$\ll 1\,\mu$Jy	$\ll 0.2\,\mu\mathrm{K_{CMB}}$
150 GHz	$< 1\,\mu$Jy	$< 0.13\,\mu\mathrm{K_{CMB}}$
100 GHz	$1 - 3\,\mu$Jy	$0.1 - 0.3\,\mu\mathrm{K_{CMB}}$

Radio point source confusion clearly should not be a problem except possibly at 100 GHz.

However, it will be necessary to survey the fields and remove the brightest radio sources – the above calculation only says that such sources are rare enough that they will not become confused. A reasonable procedure would be to first cover the entire 100 arcmin^2 with VLA or ATCA at 1.4 GHz and follow by observing the brightest sources found at 1.4 GHz with ALMA in the band of interest – very much like the way we expect to remove the brightest infrared point sources. A quick visit to the VLA and ATCA exposure calculators[18] indicates that obtaining maps of a 100 arcmin^2 cluster field at 1.4 GHz to the tens of μJy flux level needed to identify radio point sources should not be difficult. ALMA follow-up would easily find such sources, and here the cross-calibration is not so critical because the source fluxes are quite small compared to the SZ signals.

Diffuse synchrotron and free-free emission from the galaxy are expected to be well below 1 $\mu\mathrm{K_{CMB}}$ at the angular scales of interest [53], so we neglect them.

5.3 Primary CMB

Primary CMB anisotropy drops off exponentially on length scales of a few arcminutes, so CMB anisotropy should primarily be a problem for recovery of large-scale cluster structure. Fortunately, tSZ is spectrally distinguishable from CMB anisotropy, so it should be possible to remove CMB anisotropy from tSZ without any problem, provided similar $\mu\mathrm{K_{CMB}}$ sensitivities can be obtained in multiple millimeter-wave bands. kSZ is spectrally indistinguishable from CMB anisotropy. On few–10 arcmin scales, we will have to use the cluster structure as obtained from tSZ and possibly X-ray observations to provide a spatial template for separating kSZ from CMB. On smaller scales

[18] http://www.vla.nrao.edu/astro/guides/exposure/calc.html and http://www.atnf.csiro.au/observers/docs/at_sens/

– especially in the cluster core – kSZ should dominate thanks to the higher electron optical depth and the larger spatial scale separation from CMB.

5.4 Polarized Confusion

Since the sensitivity to polarized SZ effects is too poor to expect detection, we do not discuss polarized confusion sources.

6 Requirements on Telescope and Instrumentation

The above science goals, signal levels, and sensitivity expectations place the following requirements on the telescope and instrumentation:

- **Aperture size**: Not a critical requirement directly. For SZ effect measurements that resolve clusters, it is temperature (= surface brightness) sensitivity that matters, not point-source sensitivity. Reduction in size to 20 m would have little negative effect. The telescope size could be increased at no detriment to SZ observations (the SZ camera can always underilluminate) as long as there is no loss of field of view. But anything that degrades the confusion limit at higher frequencies will make it harder to remove infrared point-source confusion in the SZ bands. Indirectly, then, a scaleback to 20 m would degrade SZ sensitivity by a factor equal to the increase in the confusion limit at 350 GHz and 490 GHz.

- **Surface roughness**: Not a critical requirement. Certainly will be driven by submillimeter work. Most important effect is actually on optical loading (see next item).

- **Blockage/Loading**: At millimeter wavelengths, the sky will be so transparent as to be essentially a non-issue as far as optical loading: according to T. Herter's sensitivity spreadsheet, the zenith opacities and expected optical loading (in Kelvins assuming $T_{\rm atm} = 250\ K$) for 1 mm PWV are

frequency	τ_z	K_z
275 GHz	0.05	13 K
215 GHz	0.04	10 K
150 GHz	0.02	5 K
100 GHz	0.02	5 K

  Typical internal instrumental loading is about 10 K, and can be pushed down further with special precautions. To maximize instrumental sensitivity, then, optical loading from telescope emission, blockage, **and** diffraction should be kept quite low, at the 10K to 15K level. The working specification of a 10% emissivity telescope degrades the sensitivity at 150 GHz by a factor of about 1.5 (a factor of a bit more than 2 in integration time!) relative to 5% emissivity. Numerically, the sensitivity degrades from 190 μK$_{\rm CMB}$ s$^{1/2}$ to about 310 μK$_{\rm CMB}$ s$^{1/2}$, or from 1.4 mJy s$^{1/2}$ to 2.3 mJy s$^{1/2}$ in NEFD.

  Due to the importance of diffraction, specification of the telescope emissivity is not simply a blockage requirement; a full physical-optics calculation must be done to evaluate the true optical loading of any design. Experience with the CSO has shown that telescope loading actually **degrades** with decreasing frequency, presumably due to diffraction in the optics, from the (rather burly) feed legs, and perhaps reflection from the center of the secondary.

- **Field of View**: As explained earlier, the largest angular scale of interest is about 10 arcmin. It is well known that recovery of signals on length scales larger than the field of view in the presence of sky noise is difficult. Thus, a field of view of 10 arcmin diameter is desired, with a goal of 20 arcmin diameter to ensure even the largest clusters can be contained in the field of view.

- **Frequency Coverage**: Figure 1 indicates that, from the simple point of view of power received by a detector, the best bands for detection of tSZ are 100 and 150 GHz.. The argument becomes more solid when one recognizes that sky emission and sky noise are worse at higher frequencies. 100 GHz is actually somewhat better than 150 GHz with regard to infrared point-source confusion. But the angular resolution at 100 GHz will be degraded to about 0.66 arcmin FWHM, and 100 GHz observations will be obtained by the SZA interferometric array at CARMA, so 100 GHz is not the optimal niche for CCAT. 150 GHz seems the best choice for the primary tSZ band for CCAT.

  For point-source removal and investigation of the kSZ effect, bands at and above the tSZ null are needed. The null band obviously needs to be at 220 GHz. The higher band could be at 275 GHz or 350 GHz; there is no clear winner because both will be badly IR point-source contaminated. More detailed study is required to understand better the tradeoffs. Bands at 350 GHz and 490 GHz are desired for point-source removal. Both are desired: removal of source based on 350 GHz observations will have less systematic uncertainty on the spectral extrapolation to the SZ bands, but 490 GHz data will go deeper. The brightest sources will be removed using 350 GHz data and the dimmer ones using 490 GHz data.

- **Pointing and Tracking**: "On-the-fly" pointing need only be good to about a beam in order to make sure the target is centered well enough on the array. However, the need for precise point-source removal using observations at other wavelengths put a more stringent requirement on *reconstructed* pointing. This needs to be quantified using simulations, but, to first order, reconstructed point to better than 0.1 beam FWHM seems necessary.

- **Scan Speed**: Experience with Bolocam shows that increasing the scan speed in general improves sensitivity – the atmospheric $1/f$ noise remains roughly unchanged in frequency space as the scan speed is increased, but the astronomical signal is pushed to higher frequency. This occurs because, at the scan speeds used by Bolocam – up to 4 arcmin s^{-1}– the scan speed is much slower than the expected wind speed. Within the context of a moving screen model, one expects improvement until the scan speed is comparable to the wind speed, at which point the motion of the telescope just modulates the atmopheric turbulence more quickly. Wind speeds are of order 10 m s^{-1} at 1 km, the characteristic height of the water vapor. This corresponds to about 35 arcmin s^{-1}. Thus, scan speeds of 0.5 to 1 degree s^{-1} would be useful in minimizing the effects of sky noise, but faster scan speeds would not.

- **Spillover Fluctuations**

- **Spectroscopy**: Low-resolution ($R \sim 30 - 100$) spectroscopy over the frequency range 120–325 GHz is desirable to observe relativistic spectral corrections to the tSZ effect and to assess infrared point-source contamination. A single- or few-pixel background-limited spectrometer with 3 GHz resolution through the 120–325 GHz regime would suffice. This could sensible be split into two bands, 120-180 GHz and 190-300 GHz, to accomodate the 1:1.6 band-edge ratio for a ZSPEC-like spectrometer.

7 Discarded Alternatives

Clearly, this discussion has focused on tSZ follow-up as the main goal of a CCAT SZ instrument, with kSZ detection and surveys for tSZ and kSZ anisotropy as subsidiary goals. Here we list some other science topics and technical alternatives that have been discarded due to lack of uniqueness or sensitivity.

- **Underfilling the primary**: The confusion problem is aggravated by the very small beams we get with a 25-m telescope. Since SZ is a surface-brightness source, a smaller telescope receives the same power on a detector as CCAT, but will receive proportionately less power from point sources. Would anything be gained by underfilling the CCAT primary for SZ work? The main difficulty with this idea is that it degrades the angular resolution and thus makes CCAT non-unique. CCAT's strength is not in duplicating SPT (a 10-m dish at a better site), but in complementing the SPT surveys by doing higher angular-resolution follow-up.

- **Wide-area surveys**: Would it be sensible to conduct a wide-area blind SZ survey to a lower mass-limit than SPT can reach, making use of the smaller CCAT beams? The difficulty is that, in survey mode, where one leaves the cluster unresolved and detects total flux, the flux scales roughly as $M^{5/3}$ – one factor of cluster mass and one factor of electron temperature. A factor of 3 improvement in mass-limit over SPT to 1×10^{14} $M_\odot$ is accessible, but it is not clear if this gains one much in terms of cosmology. Reaching lower masses becomes very difficult due to the strong dependence of flux on mass and confusion noise.

  One interesting idea would be to use CCAT to characterize the SPT mass detection function very well. This is entirely sensible and is effectively subsubmed into the topic of SZ cluster follow-up.

- **Primary CMB anisotropy**: Primary CMB anisotropy is damped exponentially on few-arcminute angular scales. While some primary anisotropy is probably accessible to CCAT, it seems sensible to leave that work to APEX, ACT, and SPT, whose angular resolutions and fields of view are more well-matched to primary anisotropy. Similarly, primary CMB polarization anisotropy is best addressed by instruments with coarser angular resolution.

- **SZ polarization**: To all intents and purposes, SZ polarization is undetectable – the signal levels are 10 nK_{CMB} and below. Even seeing such a signal in one cluster would take 10^8 seconds. Scientifically, a large catalog of such clusters would be needed to extract any interesting science (redundant measures of the CMB quadrupole, transverse cluster velocities).

8 Future Work

Obviously, this document is a very simplistic first pass at establishing signal levels and angular sizes of interest. Detailed simulation work will be needed to optimize instrumentation for SZ work. Specific goals of a detailed design study should be as follows:

1. Realistic assessment of expected per-pixel sensitivities, including expected opacity distribution during which long-wavelength instruments will be used and some attempt to model sky noise and predict residual sky noise levels.

2. Use of analytic and numerical methods to predict expected thermal SZ and kinetic SZ signals and confusion noise. This should include expected cluster profiles, cluster counts and

abundance functions, expected peculiar velocities, and expected anisotropy power spectra. A realistic assessment of the effect of current theoretical uncertainties, both in predicting the dark matter power spectrum, predicting the gas physics that yields the SZ effects, and predicting the confusing source counts, should be included.

3. Optimization of samples or surveys (mass limit or flux limit) for science output.

4. Study of the effect of beam size on science output. To first order, CCAT's niche is in high-angular-resolution work, so degradation of the beam size by underillumination of the primary does not seem like the way to go. But this ought to be studied in some detail before excluding the possibility. ACT and SPT have, if anything, resolution a bit poorer than one would like; would much be gained by degrading the beam size to 0.5–0.75 arcmin?

5. More realistic assessment of confusion levels and how much short-wavelength/ALMA follow-up is needed to reduce confusion noise to reasonable levels.

6. Realistic evaluation of systematic instrumental uncertainties on separation of thermal and kinetic effects and on removal of point sources. Obviously, pointing registration, both internally to the SZ observations as well as to external (CCAT or interferometric) point-source observations is critical, as is flux cross-calibration between bands of CCAT and to interferometric measurements.

References

[1] J. E. Carlstrom, G. P. Holder, and E. D. Reese, Annu. Rev. Astro. Astroph. **40**, 643 (2002).

[2] J. F. Navarro, C. S. Frenk, and S. D. M. White, Astroph. J. **490**, 493 (1997).

[3] J. P. Henry, Astroph. J. **534**, 565 (2000).

[4] R. H. Wechsler *et al.*, Astroph. J. **568**, 52 (2002).

[5] D. H. Zhao, H. J. Mo, Y. P. Jing, and G. Börner, Mon. Not. Roy. Astron. Soc. **339**, 12 (2003).

[6] J. S. Bullock *et al.*, Mon. Not. Roy. Astron. Soc. **321**, 559 (2001).

[7] A. R. Cooray, Ph.D. thesis, University of Chicago, 2001.

[8] U. Seljak, Mon. Not. Roy. Astron. Soc. **318**, 203 (2000).

[9] E. Komatsu and U. Seljak, Mon. Not. Roy. Astron. Soc. **327**, 1353 (2001).

[10] N. Makino, S. Sasaki, and Y. Suto, Astroph. J. **497**, 555 (1998).

[11] Y. Suto, S. Sasaki, and N. Makino, Astroph. J. **509**, 544 (1998).

[12] A. J. Benson, C. Reichardt, and M. Kamionkowski, Mon. Not. Roy. Astron. Soc. **331**, 71 (2002).

[13] M. Birkinshaw, Phys. Rep. **310**, 97 (1999).

[14] D. M. Neumann and H. Bohringer, Mon. Not. Roy. Astron. Soc. **289**, 123 (1997).

[15] I. G. McCarthy, A. Babul, G. P. Holder, and M. L. Balogh, Astroph. J. **591**, 515 (2003).

[16] P. M. Motl, E. J. Hallman, J. O. Burns, and M. L. Norman, astro-ph/0502226, submitted to Astroph. J. Lett.

[17] A. C. da Silva, S. T. Kay, A. R. Liddle, and P. A. Thomas, Mon. Not. Roy. Astron. Soc. **348**, 1401 (2004).

[18] J. G. Bartlett, astro-ph/0001267, submitted to Astron. Astroph.

[19] J. P. Hughes and M. Birkinshaw, Astroph. J. **501**, 1 (1998).

[20] E. D. Reese *et al.*, Astroph. J. **533**, 38 (2000).

[21] W. H. Press and P. Schechter, Astroph. J. **187**, 425 (1974).

[22] R. K. Sheth and G. Tormen, Mon. Not. Roy. Astron. Soc. **308**, 119 (1999).

[23] A. Jenkins *et al.*, Mon. Not. Roy. Astron. Soc. **321**, 372 (2001).

[24] G. Holder, Z. Haiman, and J. J. Mohr, Astroph. J. Lett. **560**, L111 (2001).

[25] C. L. Bennett *et al.*, Astroph. J. Suppl. **148**, 1 (2003).

[26] G. P. Holder *et al.*, Astroph. J. **544**, 629 (2000).

[27] A. C. Peel, astro-ph/0501098, submitted to Astroph. J.

[28] Z. Haiman, J. J. Mohr, and G. P. Holder, Astroph. J. **553**, 545 (2001).

[29] A. E. Schulz and M. White, Astroph. J. **586**, 723 (2003).

[30] R. A. Battye and J. Weller, astro-ph/0410392, submitted to Mon. Not. Roy. Astron. Soc.

[31] J.-B. Melin, J. G. Bartlett, and J. Delabrouille, Astron. Astroph. **429**, 417 (2005).

[32] A. Refregier, E. Komatsu, D. N. Spergel, and U. Pen, Phys. Rev. D **61**, 1230¡01 (2000).

[33] A. Refregier and R. Teyssier, Phys. Rev. D **66**, 043002 (2002).

[34] U. Seljak, J. Burwell, and U. Pen, Phys. Rev. D **63**, 063001 (2001).

[35] V. Springel, M. White, and L. Hernquist, Astroph. J. **549**, 681 (2001).

[36] W. Hu, Astroph. J. **529**, 12 (2000).

[37] E. Komatsu and U. Seljak, Mon. Not. Roy. Astron. Soc. **336**, 1256 (2002).

[38] K. M. Huffenberger and U. Seljak, astro-ph/0408066, submitted to New Astron.

[39] Y. B. Zeldovich and R. A. Sunyaev, Sov. Astron. Lett. **6**, 285 (1980).

[40] C. L. Bennett *et al.*, Astroph. J. Lett. **464**, L1 (1996).

[41] R. A. Sunyaev and I. B. Zeldovich, Mon. Not. Roy. Astron. Soc. **190**, 413 (1980).

[42] Y. Rephaeli, Astroph. J. **445**, 33 (1995).

[43] A. Challinor and A. Lasenby, Astroph. J. **499**, 1 (1998).

[44] N. Itoh, Y. Kohyama, and S. Nozawa, Astroph. J. **502**, 7 (1998).

[45] S. Nozawa, N. Itoh, and Y. Kohyama, Astroph. J. **508**, 17 (1998).

[46] S. Y. Sazonov and R. A. Sunyaev, Astroph. J. **508**, 1 (1998).

[47] N. Itoh, S. Nozawa, and Y. Kohyama, Astroph. J. **533**, 588 (2000).

[48] S. Nozawa, N. Itoh, Y. Kawana, and Y. Kohyama, Astroph. J. **536**, 31 (2000).

[49] N. Itoh, Y. Kawana, S. Nozawa, and Y. Kohyama, Mon. Not. Roy. Astron. Soc. **327**, 567 (2001).

[50] N. Itoh and S. Nozawa, Astron. Astroph. **417**, 827 (2004).

[51] S. Nozawa, N. Itoh, and Y. Kohyama, astro-ph/0501114, submitted to Astroph. J.

[52] A. W. Blain, private communication.

[53] M. Tegmark and G. Efstathiou, Mon. Not. Roy. Astron. Soc. **281**, 1297 (1996).

[54] ALMA Sensitivity Calculator, http://www.eso.org/projects/alma/science/bin/sensitivity.html.

[55] L. Toffolatti *et al.*, Mon. Not. Roy. Astron. Soc. **297**, 117 (1998).